Optimization-Based Variable Impedance Control of Robotic Manipulator for Medical Contact Tasks

Junling Fu, *Graduate Student Member, IEEE*, Ilaria Burzo, Elisa Iovene, *Graduate Student Member, IEEE*, Jianzhuang Zhao, *Student Member, IEEE*, Giancarlo Ferrigno, *Senior Member, IEEE*, and Elena De Momi, *Senior Member, IEEE*

***Abstract*— This work presents an optimization-based variable impedance control strategy for controlling a robotic manipulator in medical contact tasks. Specifically, the optimal robot stiffness for performing the medical contact task is obtained using online Quadratic programming (QP). In the meantime, an energy tank approach is incorporated into the control loop to regulate the system's passivity. To verify the performance of the proposed strategy, experiments are conducted on both *"static"* and *"scanning"* medical contact tasks, utilizing materials with different properties, different magnitudes of contact forces, as well as uneven conditions with a human torso phantom model and slope surface. The maximum Root Mean Square Error (RMSE) of force tracking with the proposed method in the *"static"* and *"scanning" tasks*, across all setups, is 0.88 and 0.5 N, respectively. The experiment results demonstrate the superiority of the proposed control strategy compared with traditional manual contact and constant stiffness (CS) impedance control-based ones. The proposed control framework is promising to be integrated into robot-assisted medical contact tasks, for example, the palpation and Ultrasound (US) imaging scenarios.**

***Index Terms*— Contact-rich task, force measurement, medical robot, optimization control, variable impedance control.**

I. Introduction

NUMEROUS medical scenarios involve contact tasks, such as palpation [1] and Ultrasound (US) imaging [2], [3]. During these tasks, the surgeon needs to apply appropriate force to the patient's body or organ and smoothly slide on the surface to perform diagnosis simultaneously. For example, physicians employ controlled force to access the texture, tenderness, or abnormalities in organs or tissues in palpation medical scenarios [1]. Similarly, the sonographer must manually maintain optimal contact force to ensure acoustic coupling between the US probe and the patient's body. This enables acquiring high-quality US images for diagnosis [2].

Manuscript received 25 August 2023; revised 26 January 2024; accepted 19 February 2024. Date of publication 1 March 2024; date of current version 13 March 2024. This work was supported in part by the China Scholarship Council (CSC). The Associate Editor coordinating the review process was Dr. Bruno Andò. *(Junling Fu and Ilaria Burzo contributed equally to this work.) (Corresponding author: Junling Fu.)*

Junling Fu, Ilaria Burzo, Elisa Iovene, Giancarlo Ferrigno, and Elena De Momi are with the Department of Electronics, Information and Bioengineering, Politecnico di Milano, 20133 Milan, Italy (e-mail: junling.fu@polimi.it).

Jianzhuang Zhao is with the Department of Electronics, Information and Bioengineering, Politecnico di Milano, 20133 Milan, Italy, and also with the Human-Robot Interfaces and Interaction Laboratory, Istituto Italiano di Tecnologia, 16163 Genoa, Italy.

Digital Object Identifier 10.1109/TIM.2024.3372209

The traditional manual execution of medical contact tasks presents several challenges for surgeons or clinicians during the task execution, including the steep learning curve for novice clinicians, high workload, and infection issues. By leveraging the high positioning capability, improved ergonomics, and infection avoidance, robots have been seamlessly integrated into various medical applications, holding tremendous potential for enhancing the precision and dexterity of clinicians while minimizing patient trauma [4], [5], [6].

The integration of robotic systems in medical contact tasks provides several compelling benefits, such as standardized results, alleviating the surgeon's workload, and infection prevention. For instance, a fully autonomous system for robot-assisted US scanning tasks was implemented in [7], where the clinicians performed demonstrations and the robot reproduced the learned results repetitively, relieving the clinician's workload. However, several critical concerns persist, such as contact force control, system stability, user comfort, and safety issues, especially in unstructured and dynamic environments, and interaction with deformable objects [8].

Significant advancements have been achieved in robot-assisted medical contact tasks, emphasizing safety, contact force handling capabilities, and system stability. Customized mechanical structures have been designed to perform medical contact tasks considering the simple control strategy and robustness. For instance, Bao et al. [9] proposed a novel robot mechanism that integrated a force control mechanism, a force/torque measurement mechanism, and an adaptive control strategy to assist sonographers in performing efficient US scanning tasks. Tan et al. [10] designed a dual robotic arms system for clamping the US device. Each robotic arm had five Degree-of-Freedoms (DoFs), comprising three orthogonal translational axes and two orthogonal rotation axes. However, the mechanical structure was usually designed for a specified task, and the complicated structure increased the cumbersome of the hardware part of the robotic system.

In recent years, general robotic manipulators have been widely employed to hold surgical tools to execute various medical contact tasks [4]. For instance, the Universal Robot (UR) has successfully integrated an US probe for precise medical scanning tasks, capitalizing on the system's remarkable precision and maneuverability [11]. The explicit force or hybrid position-force control was typically adopted in robot-assisted contact tasks considering the straightforward

control schemes [11]. Nevertheless, the overall stability of the system remains a challenge, particularly in dynamic or unstructured environments, potentially resulting in harm to the human organs or anatomical structure.

To enhance safety during the task execution, the impedance controller has been implemented and proven beneficial for contact manipulation tasks [12], as well as human-robot collaboration [13]. For example, Jiang et al. [14] integrated stiffness estimation and regression to estimate the dynamic stiffness of the deformable phantom. Afterward, a quadratic function was employed to model the flexibility priorities of the elastic tissue. Subsequently, the stiffness value was set in the Cartesian impedance controller of the robotic manipulator. Moreover, Tan et al. [15] investigated the impact of displacement on the contact force applied to the patient's body during the medical scanning task using a robotic manipulator incorporated with an admittance controller. Typically, accurate and real-time measurement and stiffness estimation are challenging, particularly in deformable contact and unstructured environments [8].

To empower both force-tracking capabilities and compliance of the robotic system, variable impedance control techniques have been explored. Biagiotti et al. [16] investigated a human-in-the-loop adjustment strategy. They proposed an online regulation strategy using the sEMG signals. In [17], an alternative approach using a Reinforcement Learning (RL) algorithm was introduced. The RL algorithm was adopted to learn a variable impedance control policy in the robot's end-effector space for performing contact-rich tasks. However, the RL training process is typically time-consuming and a reliable simulation environment is indispensable. Roveda et al. [18] investigated the online optimization strategy to find the optimal parameters for force-tracking. The optimization process was formulated as a linear quadratic regulator (LQR) problem to interact with a partially unknown environment. Similarly, the hybrid offline robot learning and online optimization control framework were implemented for robot-assisted contact tasks [19]. However, the deformation of the environment and closed-loop force control was not considered.

To address the aforementioned issues, this work presents an optimization-based control framework for medical contact tasks. The main contributions are summarized as follows.

1) A closed-loop variable impedance control strategy is proposed to track the desired contact force in medical scenarios using Quadratic programming (QP).
2) An energy tank is utilized to ensure the system passivity of the proposed optimization-based control strategy.

II. Preliminaries

A. Cartesian Impedance Controller of Robotic Manipulator

The dynamic model of a n-DoFs serial robotic manipulator in the joint space is formulated as

$$\boldsymbol{M}(\boldsymbol{q})\ddot{\boldsymbol{q}} + \boldsymbol{C}\left(\boldsymbol{q}, \dot{\boldsymbol{q}}\right)\dot{\boldsymbol{q}} + \boldsymbol{G}(\boldsymbol{q}) - \boldsymbol{\tau}_{\text{ext}} = \boldsymbol{\tau}_{\boldsymbol{cmd}} \tag{1}$$

where $\boldsymbol{M} \in \mathbb{R}^{n\times n}$, $\boldsymbol{C} \in \mathbb{R}^{n\times n}$, and $\boldsymbol{G} \in \mathbb{R}^{n}$ are the symmetric and positive definite mass matrix, the Coriolis and Centrifugal matrix, and the gravitational vector, respectively. $\boldsymbol{q}, \dot{\boldsymbol{q}}, \ddot{\boldsymbol{q}} \in \mathbb{R}^{n}$ are the angels, velocities, and accelerations, $\boldsymbol{\tau}_{\text{ext}} \in \mathbb{R}^{n}$ and $\boldsymbol{\tau}_{\text{cmd}} \in \mathbb{R}^{n}$ are the external and command torques vectors. In Cartesian space with m-DoFs, (1) is reformulated as

$$\boldsymbol{M}(\boldsymbol{x})\ddot{\boldsymbol{x}} + \boldsymbol{C}\left(\boldsymbol{x}, \dot{\boldsymbol{x}}\right)\dot{\boldsymbol{x}} + \boldsymbol{F}_{\boldsymbol{g}}(\boldsymbol{x}) - \boldsymbol{F}_{\text{ext}} = \boldsymbol{F}_{\text{cmd}} \tag{2}$$

where $\boldsymbol{x} \in \mathbb{R}^{m}$, $\dot{\boldsymbol{x}} \in \mathbb{R}^{m}$, and $\ddot{\boldsymbol{x}} \in \mathbb{R}^{m}$ are the measured position, velocity, and acceleration terms. $\boldsymbol{F}_{\text{ext}} \in \mathbb{R}^{m}$, $\boldsymbol{F}_{\boldsymbol{g}} \in \mathbb{R}^{m}$, and $\boldsymbol{F}_{\text{cmd}} \in \mathbb{R}^{m}$ are the external, gravity, and wrench.

The contact force $\boldsymbol{F}_{\text{ext}} \in \mathbb{R}^{m}$ in (2) between the robot and the environment can be approximately calculated by

$$\boldsymbol{F}_{\text{ext}} = \boldsymbol{M}\ddot{\tilde{\boldsymbol{x}}} + \boldsymbol{K}_{\boldsymbol{c}}\tilde{\boldsymbol{x}} + \boldsymbol{D}_{\boldsymbol{c}}\dot{\tilde{\boldsymbol{x}}} \tag{3}$$

$$\tilde{\boldsymbol{x}} = \boldsymbol{x}_{\text{des}} - \boldsymbol{x}_{\text{msr}} \tag{4}$$

where $\tilde{\boldsymbol{x}} \in \mathbb{R}^{m}$, $\dot{\tilde{\boldsymbol{x}}} \in \mathbb{R}^{m}$, and $\ddot{\tilde{\boldsymbol{x}}} \in \mathbb{R}^{m}$ are the Cartesian pose error, velocity error, and acceleration terms. $\boldsymbol{M} \in \mathbb{R}^{m\times m}$, $\boldsymbol{K}_{\boldsymbol{c}} \in \mathbb{R}^{m\times m}$ and $\boldsymbol{D}_{\boldsymbol{c}} \in \mathbb{R}^{m\times m}$ are the positive definite mass, stiffness, and damping parameters, respectively. $\boldsymbol{x}_{\text{des}} \in \mathbb{R}^{m}$ and $\boldsymbol{x}_{\text{msr}} \in \mathbb{R}^{m}$ are the desired and measured current robot position.

B. Passivity of the Robotic System

In terms of energy, a dynamic system is passive if it does not generate internal energy [20], which is represented by $E_i = E_{\text{out}} - E_{\text{in}} \leq 0$. Where E_{out} and E_{in} represent the energy of output and input to the system. In (3), the energy of the system, V, is calculated by the sum of the kinetic energy, V_k, and elastic potential energy, V_e, which is expressed by

$$V\left(\tilde{\boldsymbol{x}}, \dot{\tilde{\boldsymbol{x}}}\right) = \underbrace{\frac{1}{2}\dot{\tilde{\boldsymbol{x}}}^{T}\boldsymbol{M}(\boldsymbol{x})}_{V_k} + \underbrace{\frac{1}{2}\tilde{\boldsymbol{x}}^{T}\boldsymbol{K}_{\boldsymbol{c}}\tilde{\boldsymbol{x}}}_{V_e}. \tag{5}$$

Substituting (3) into (5), and considering $\dot{\boldsymbol{M}}(\boldsymbol{x}) - 2C(\tilde{\boldsymbol{x}}, \dot{\tilde{\boldsymbol{x}}})$ is a skew-symmetric one [21], we have

$$\dot{V} = \dot{\tilde{x}}^{T}\boldsymbol{F}_{\boldsymbol{ext}} - \dot{\tilde{\boldsymbol{x}}}^{T}\boldsymbol{D}_{\boldsymbol{c}}\dot{\tilde{\boldsymbol{x}}} \leq \dot{\tilde{x}}^{T}\boldsymbol{F}_{\boldsymbol{ext}} \tag{6}$$

which implies that the system is strictly passive with the power port $(\boldsymbol{F}_{\text{ext}}, \dot{\tilde{\boldsymbol{x}}})$ and fulfilling the passivity condition

$$V(t) - V(0) \leq \int_{0}^{t} \dot{\tilde{\boldsymbol{x}}}^{T}(\tau)\boldsymbol{F}_{\text{ext}}(\tau)d\tau \tag{7}$$

where $V(t)$ and $V(0)$ are the energy at time t and $t = 0$.

III. Proposed Optimization Control Strategy

A. QP-Based Online Robot Stiffness Optimization

The proposed block diagram is shown in Fig. 1. The external contact force $\boldsymbol{F}_{\text{ext}}$ calculated by (3) is regulated to track the desired contact force $\boldsymbol{F}_{\text{des}}$, via an optimization problem

$$\min_{\boldsymbol{K}_{\text{car}}\in\mathbb{R}^{m\times m}} \frac{1}{2}\sum_{n=1}^{N}\left\|\boldsymbol{F}_{\boldsymbol{ext}}{}^{i} - \boldsymbol{F}_{\text{des}}\right\|^{2}. \tag{8}$$

Then, the force-tracking error, $\boldsymbol{F}_{\text{err}} \in \mathbb{R}^{m}$, which is acquired by an external force/torque sensor and recorded as $\boldsymbol{F}_{\text{msr}} \in \mathbb{R}^{m}$, is added to formulate the closed-loop control

$$\boldsymbol{F}_{\text{err}} = \boldsymbol{F}_{\text{des}} - \boldsymbol{F}_{\text{msr}} \tag{9}$$

where $\boldsymbol{F}_{\text{des}}, \boldsymbol{F}_{\text{msr}} \in \mathbb{R}^{m}$ are the desired and measured contact forces, respectively. Hence, a novel QP-based approach to

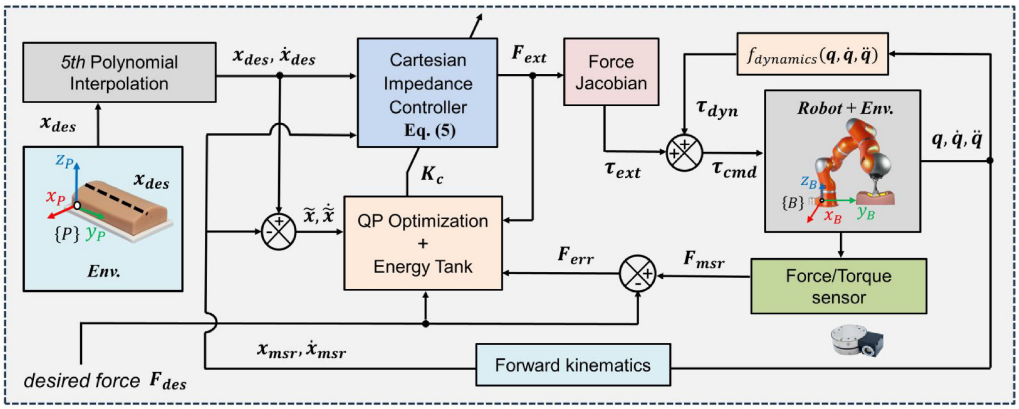

Fig. 1. Block diagram of the proposed framework; $\boldsymbol{F}_{\text{des}}$ and $\boldsymbol{x}_{\text{des}}$ are initialized as input. $\{\boldsymbol{P}\}$ and $\{\boldsymbol{B}\}$ represent the phantom and the robot base coordinate systems, respectively. The dynamics of the robotic manipulator $f_{\text{dynamic}}(\boldsymbol{q}, \dot{\boldsymbol{q}}, \ddot{\boldsymbol{q}})$ is compensated. The QP optimization calculates the optimal stiffness $\boldsymbol{K}_c$ for the task, and is regulated by the energy tank to ensure the system's passivity. $\boldsymbol{F}_{\text{err}}$ is considered to achieve closed-loop control.

online optimize the stiffness is proposed and aims at finding the optimal stiffness $\boldsymbol{K}_c(t)$ at time t, which is expressed as

$$\min_{\boldsymbol{K}_{\text{car}} \in \mathbb{R}^{m\times m}} \frac{1}{2}\sum_{n=1}^{N}\left(\left\|\boldsymbol{F_{ext}}^n - \left[\boldsymbol{F}_{\text{des}} + \alpha \boldsymbol{F}_{\text{err}}{}^n\right]\right\|_Q^2 + \|\boldsymbol{K_c}^n - \boldsymbol{K}_{\min}\|_R^2\right)$$
$$\text{s.t. } \boldsymbol{K}_{\min} \le \boldsymbol{K_c} \le \boldsymbol{K}_{\max}$$
$$0 \le \|\boldsymbol{F}_{\text{ext}}\| \le \boldsymbol{F}_{\max} \tag{10}$$

where N is the window length, and α is the gain, $\boldsymbol{Q}$ and $\boldsymbol{R} \in \mathbb{R}^{m\times m}$ are the weighting matrices. $\boldsymbol{K}_{\min}$, $\boldsymbol{K}_{\max}$, and $\boldsymbol{F}_{\max}$ are the minimal, maximum stiffness, and maximum force.

B. Energy Tank-Enhanced System Passivity

The stiffness $\boldsymbol{K_c}(t)$ of the robotic manipulator calculated from the QP formulation in (10) is time-varying, which could cause the nonpassive behavior of the system. Specifically, for a variable stiffness value, the Cartesian impedance controller of the robotic system, (3) is expressed as [21]

$$\dot{V} = \dot{\tilde{\boldsymbol{x}}}^T \boldsymbol{F_{ext}} + \left[\frac{1}{2}\tilde{\boldsymbol{x}}^T \dot{\boldsymbol{K}}_c \tilde{\boldsymbol{x}} - \dot{\tilde{\boldsymbol{x}}}^T \boldsymbol{D}_c \dot{\tilde{x}}\right]. \tag{11}$$

However, the sign of the second term in the squared brackets of (11) cannot be guaranteed due to the existence of the variable stiffness term, which probably causes the nonpassive behavior of the system. The robot variable stiffness, $\boldsymbol{K_c}(t)$, can be considered including two parts, namely the constant stiffness (CS) term $\boldsymbol{K}_{\text{cons}} \in \mathbb{R}^{m\times m}$ and the time-varying term $\boldsymbol{K_v}(t) \in \mathbb{R}^{m\times m}$, hence the robot's variable Cartesian stiffness is represented as $\boldsymbol{K_c(t)} = \boldsymbol{K}_{\text{cons}} + \boldsymbol{K_v}(t)$.

The time-varying term $\boldsymbol{K_v}(t)$ could cause the system's instability [21]. To ensure the system passivity, the energy tank approach is adopted [21]. The energy storage function, $T(x_t)$, is formulated as $T(x_t) = (1/2)x_t^2$. Where $x_t \in \mathbb{R}$ is the tank state and $T(x_t)$ is the stored energy. For the Cartesian impedance controller, the power port $(\boldsymbol{F}_{\text{ext}}, \dot{\tilde{\boldsymbol{x}}})$ of the system does the energy exchange stored in the tank with the external environment. The dynamics of the energy tank can be formulated as

$$\dot{x}_t x_t = \sigma \dot{\tilde{\boldsymbol{x}}}^T \boldsymbol{D_c} \dot{\tilde{\boldsymbol{x}}} - \omega^T \dot{\tilde{\boldsymbol{x}}}. \tag{12}$$

Additionally, the maximum available energy in the tank, $E_{\max}$, should be regulated to avoid the singularity of the system, as described in [22]. Hence, the constant value $\sigma \in \{0, 1\}$ is set to enable and disable the energy dissipation to avoid exceeding the up-energy boundary, $E_{\max}$, which is

$$\sigma = \begin{cases} 1, & \text{if } T \le E_{\max} \\ 0, & \text{otherwise} \end{cases}$$
$$\omega(t) = \begin{cases} -\boldsymbol{K_v}(t)\tilde{x}, & \text{if } T \ge E_{\min} \\ 0, & \text{otherwise.} \end{cases} \tag{13}$$

Besides, some energy should be kept in the tank to avoid singularities (i.e., $x_t \neq 0$). It is necessary to set a low boundary threshold $E_{\min} > 0$ for initializing the tank. Eventually, the dynamics of the energy in the tank are formulated as

$$\dot{T}(x_t) = \begin{cases} \sigma \dot{\tilde{\boldsymbol{x}}}^T \boldsymbol{D_c} \dot{\tilde{\boldsymbol{x}}} + \tilde{\boldsymbol{x}}^T \boldsymbol{K_v}(t) \tilde{\boldsymbol{x}}, & \text{if } T \ge E_{\min} \\ \sigma \dot{\tilde{\boldsymbol{x}}}^T \boldsymbol{D_c} \dot{\tilde{\boldsymbol{x}}}, & \text{otherwise.} \end{cases} \tag{14}$$

Eventually, the QP-based online optimization problem with multiple constraints can be rewritten as

$$\min_{\boldsymbol{K}_{\text{car}} \in \mathbb{R}^{m\times m}} \frac{1}{2}\sum_{n=1}^{N}\left(\left\|\boldsymbol{F_{ext}}^n - \left[\boldsymbol{F}_{\text{des}} + \alpha \boldsymbol{F_{err}}^n\right]\right\|_Q^2 + \|\boldsymbol{K_c}^n - \boldsymbol{K}_{\min}\|_R^2\right)$$
$$\text{s.t. } \boldsymbol{K}_{\min} \le \boldsymbol{K_c} \le \boldsymbol{K}_{\max}$$
$$0 \le \|\boldsymbol{F}_{\text{ext}}\| \le \boldsymbol{F}_{\max}$$
$$T \ge E_{\min}. \tag{15}$$

C. Implementation Details

1) Cartesian Impedance Controller: Considering the low-speed, $\boldsymbol{M}\ddot{\tilde{\boldsymbol{x}}}$ in (3) is neglected for simplification. $\boldsymbol{D_c}$ in (3) is set as the critical one $\boldsymbol{D_c} = 2 * \xi * (\boldsymbol{K_c})^{1/2}$. Where $\xi \in [0, 1]$ is the damping coefficient, and $\xi = 0.707$ is adopted. In this work, the displacement $\tilde{\boldsymbol{x}}$ in (3) of the cartesian impedance controller is appropriately set to ensure safety during the contact tasks [10] and calculated by

$$\tilde{\boldsymbol{x}} = \frac{1}{2} * \left(\frac{\boldsymbol{F}_{\text{des}}}{\boldsymbol{K}_{\min}} + \frac{\boldsymbol{F}_{\text{des}}}{\boldsymbol{K}_{\max}}\right) \tag{16}$$

Algorithm 1 Energy Tank-Enhanced System Passivity

while Optimization loop is active **do**
  Initialize energy in the tank $T(x_0) = T_0 = \varepsilon$
  if $\dot{T}(x_t) \leq E_{\max}$ **then**
    $\sigma = 1$
  else
    $\sigma = 0$
  end if
  if $\dot{T}(x_t) > \varepsilon$ **then**
    $\boldsymbol{K}_c = \boldsymbol{K}_{\text{cons}} + \boldsymbol{K}_v$
    $\dot{T}(x_t) = \sigma \tilde{\boldsymbol{x}} \boldsymbol{D}_c \dot{\tilde{\boldsymbol{x}}} + \tilde{\boldsymbol{x}} \boldsymbol{K}_v \dot{\tilde{\boldsymbol{x}}}$
  else
    $\boldsymbol{K}_{\text{car}} = \boldsymbol{K}_{\text{min}}$
    $\dot{T}(x_t) = \sigma \tilde{\boldsymbol{x}} \boldsymbol{D}_c \dot{\tilde{\boldsymbol{x}}}$
  end if
  $T(x_t) = T(x_{t-1}) + \dot{T}(x_t)\Delta t$
end while

where $\boldsymbol{K}_{\min}$ and $\boldsymbol{K}_{\max}$ are the adopted minimum and maximum stiffness [14]. Specifically, the values are approximately set in the range of [125, 500] N/m [14].

2) QP-Based Optimization: In our work, the optimization is in real-time. Hence, the time window length in (15) is set as $N = 1$. Then, the objective optimization function, $\boldsymbol{f}$, to calculate the optimal robot stiffness $\boldsymbol{K}_c$ is expressed as

$$\boldsymbol{f} = \frac{1}{2}\left(\boldsymbol{Q} * \tilde{\boldsymbol{x}}^2 + \boldsymbol{R}\right)\boldsymbol{K}_c{}^2 + \left[\boldsymbol{Q} * \tilde{\boldsymbol{x}}\left(\boldsymbol{D}_d \dot{\tilde{\boldsymbol{x}}} - \boldsymbol{F}_{\text{des}}\right) - \boldsymbol{R} * \boldsymbol{K}_{\min}\right] * \boldsymbol{K}_c. \quad (17)$$

Equation (17) is further formulated as the general QP express

$$\min_{\boldsymbol{x} \in \mathbb{R}^m} f(\boldsymbol{x}) = \frac{1}{2}\boldsymbol{x}^T \boldsymbol{A}\boldsymbol{x} + \boldsymbol{b}^T \boldsymbol{x} \quad (18)$$

where $\boldsymbol{x} \in \mathbb{R}^m$ and $\boldsymbol{b} \in \mathbb{R}^m$ are vectors, and $\boldsymbol{A} \in \mathbb{R}^{m \times m}$ is the symmetric matrix.

3) Energy Tank: The Cartesian impedance controller and the energy tank are implemented discreetly as

$$T(x_t) = T(x_{t-1}) + \dot{T}(x_t)\Delta t \quad (19)$$

where Δt is the sampling time of the control loop. To avoid the singularity of the energy tank, the energy in the tank is initialized with a constant value T_0, also representing the lowest threshold ε in the energy tank. Considering the human tissues vary from [125, 500] N/m [14], [23], the optimized stiffness (OS) value in (15) is regulated within the range of [100, 500] N/m. Thus, the CS value is step as $K_{\text{cons}} = K_{\min} =$ 100 N/m. More details of the energy tank implementation are summarized in Algorithm 1.

IV. Experimental Setup

A. System Implementation

1) Hardware System: The system components are shown in Fig. 2. In detail, a 7-DoFs serial robotic manipulator (LWR 4+, KUKA, Germany) is adopted as the holder of the medical contact probe; A 6-axis force/torque sensor (M3815C-SN2537, SRI, China) is mounted to the robot end-effector to measure the real-time contact force. M3815C exhibits the capability to precisely measure force and torque within the ranges of 0–130 N and 0–10 Nm, respectively. In addition, a 3-D-printed linear US probe (L12-5L40S-3, TeleMed, Vilnius, Lithuania) is attached to the robot end-effector.

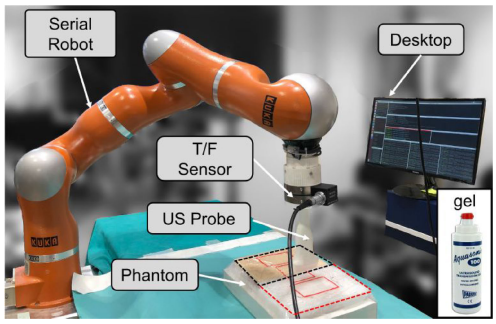

Fig. 2. System components of the proposed framework.

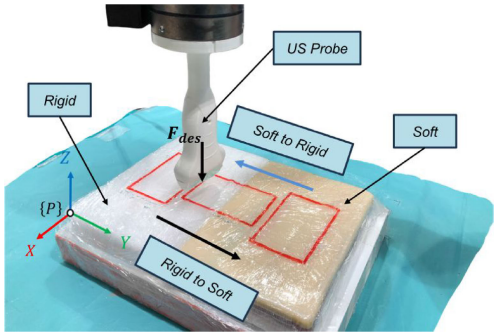

Fig. 3. Illustration of the medical contact tasks in the experiments.

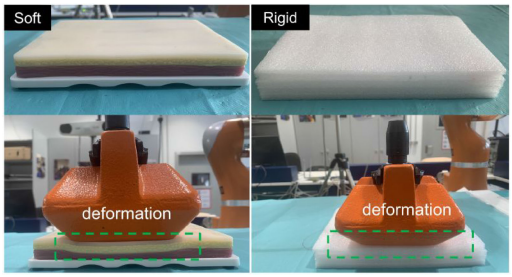

Fig. 4. Two phantoms with different materials in the experiments.

2) Software System: The Ubuntu 16.04 LTS version incorporates the robot operating system (ROS) Kinetic version is employed to facilitate the data communication and control of the robot through the Fast Research Interface (FRI) Library. In addition, the QP-BLEIC solver provided by the ALGLIB library[1] is adopted for the QP online optimization of (15). Additionally, the sensor records and measures the contact force/torque during the task execution.

B. Experiment Protocol

In Fig. 3, the contact tasks experiments are conducted to contact these two phantoms with different materials (Soft and rigid) and track the desired force $\boldsymbol{F}_{\text{des}}$. In Fig. 4, the *"soft"* one is an artificial soft tissue, and the *"rigid"* one is made of foam and a bit harder but still deformable during the contact.

[1]https://www.alglib.net/quadratic-programming/

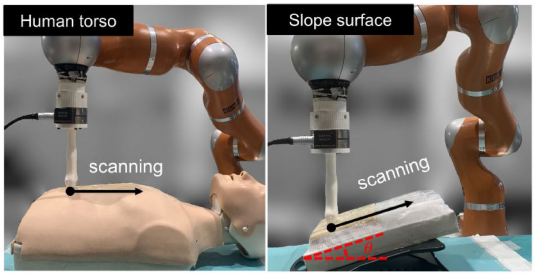

Fig. 5. Experiment setups in contact tasks with uneven conditions.

The desired contact forces are set at three different levels as $\boldsymbol{F}_{\text{des}} = [7, 10, 15]$ N, and the scanning speed is set as 8 mm/s, which is defined as refers to the US imaging task scanning speed [10], [14], [23]. Furthermore, to investigate the robustness of the proposed framework, experiments are also implemented with the setups of scanning from the *"rigid to soft"* (R2S) and from *"soft to rigid"* (S2R), respectively. Eventually, 12 contact tasks are defined.

In the contact experiment, the desired contact force is regulated along the Z-axis (See Fig. 3). The contact task execution is divided into the following three steps.

1) *Step 1*: The *"initialization phase,"* the robot performs the initialization of position and force $\boldsymbol{F}_{\text{des}}$ within 5 s.
2) *Step 2*: The *"holding phase,"* last for 5 s, during which the robot stays still and tracks the desired force $\boldsymbol{F}_{\text{des}}$.
3) *Step 3*: The *"scanning phase,"* the robot performs the scanning task on the phantom, which is 80 mm in length along the Y-axis within 10 s while tracking the force $\boldsymbol{F}_{\text{des}}$.

Furthermore, the other two modalities are implemented to perform the contact task for comparison, namely: 1) manual scan (MS); 2) CS and the proposed strategy is recorded as; and 3) OS.

1) The MS modality, the orientation of the probe was fixed, and the stiffness along the translation movement (X-, Y-, and Z-axis) can be freely manipulated by the human operator with the compensation of the robot gravity. Six subjects were invited to participate in the experiments with six repetitions for each subtask. The measured force information $\boldsymbol{F}_{\text{msr}}$ is displayed on the screen to help the user adjust the contact force during the task execution.
2) The CS modality, a high CS value of 2500 N/m is set along the X- and Y-axis for the scanning, and the stiffness of in the Cartesian impedance controller along the Z-axis is 150 N/m.
3) The OS modality, the same constant high stiffness value of 2500 N/m is used along the X- and Y-axis as CS modality for precise robot position control, and the stiffness along the Z-axis is optimized to track the desired contact force $\boldsymbol{F}_{\text{des}}$ using the proposed strategy.

In addition, another experiment is implemented under uneven conditions, namely, the *"human torso phantom"* and the *"slope"* surfaces. In Fig. 5, the *"human torso phantom"* is made of a plastic material covered by a thin layer of silicone material, and the surface is uneven, the scanning movement is 16 cm with 20 s; The *"slope"* angle θ for the XY plane is approximately 25°. This setup can be considered as the scenario with external disturbance along the Z-axis, the *"initialization phase"* and *"scanning phase"* last for 5 and 10 s, with 80 mm length scanning along the Y-axis.

TABLE I
RMSE_{ERR} RESULTS WITH DIFFERENT CONTACT PHASES AND MODALITIES

Force	Setups	Holding (N)		Scanning (N)			
		Rigid	Soft	Rigid	Soft	R2S	S2R
7N	MS	0.47	0.59	1.51	1.46	1.30	1.09
	CS	2.90	3.42	1.48	1.57	1.55	2.04
	OS	0.60	0.52	0.36	0.39	0.40	0.39
10N	MS	0.55	0.48	1.05	1.52	1.37	1.38
	CS	2.90	3.81	1.48	1.64	1.72	2.12
	OS	0.78	0.69	0.44	0.46	0.48	0.54
15N	MS	0.58	0.46	2.40	1.98	2.13	2.30
	CS	3.30	2.65	2.66	1.49	2.30	1.64
	OS	0.88	0.72	0.48	0.47	0.57	0.43

C. Performance Metrics

In this work, the Median value and the Standard Deviation (SD) SD_{err} of the measured force ${\boldsymbol{F}_{\text{msr}}}^t$ by the force/torque sensor at the sampling time t is calculated as

$$\text{SD}_{\text{err}} = \sqrt{\frac{1}{T}\sum_{t=1}^{T}\left({\boldsymbol{F}_{\text{msr}}}^t - \boldsymbol{F}_{\text{avg}}\right)^2} \tag{20}$$

where T is the number of samplings and $\boldsymbol{F}_{\text{avg}}$ is the average of the sampled data. In addition, the Root Mean Squared Error (RMSE) of the desired force RMSE_{err} is calculated by

$$\text{RMSE}_{\text{err}} = \sqrt{\frac{1}{T}\sum_{t=1}^{T}\left({\boldsymbol{F}_{\text{msr}}}^t - \boldsymbol{F}_{\text{des}}\right)^2}. \tag{21}$$

Afterward, the nonparametric statistical analysis is implemented to compare the results in different contact modalities with the Wilcoxon Rank-Sum test exploited. A significant difference is assessed with a $p-\text{value} < 0.05$, ($*$, $p < 0.05$).

V. EXPERIMENTAL RESULTS

A. Experiment Results in Static Phase of Contact Task

This part presents the experiment results during the *"static phase."* Fig. 6 illustrates the detailed force-tracking curves (the desired contact force, $\boldsymbol{F}_{\text{des}}$, is 10 N) during the whole task execution with all the experiment setups mentioned in Section IV-B. Specifically, the static phase force-tracking curves are the areas with gray backgrounds in Fig. 6, and the sampling time duration lasts for 5 s and is in the range of 5–10 s, as mentioned above *"holding phase."*

As shown in Fig. 6, in the MS results (top row in Fig. 6), the human operator adjusted the contact force for 0–5 s and then held the probe for 5 s to track the desired contact force. However, significant variations were still observed. In the middle row of Fig. 6, the robot did the initialization with the first 5 s, and then maintaining the desired contact force, more stable contact forces were observed, and no significant oscillations occurred. However, larger tracking errors still existed since the environment stiffness was difficult to measure

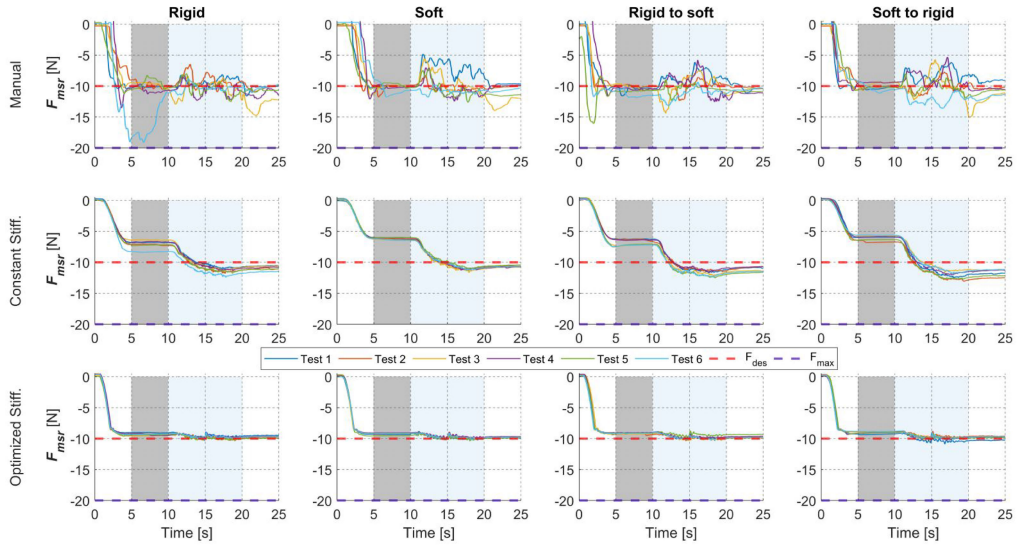

Fig. 6. Experimental results of the measured contact force using the force sensor with $\boldsymbol{F}_{\text{des}} = 10$ N, 6 repetitions are performed for each task.

TABLE II

STATISTICAL ANALYSIS OF THE RMSE_{ERR} IN THE CONTACT TASKS

Force	Setups	Holding		Scanning			
		Rigid	Soft	Rigid	Soft	R2S	S2R
7N	MS vs OS	–	–	*	*	*	*
	CS vs OS	*	*	*	*	*	*
10N	MS vs OS	–	–	*	*	*	*
	CS vs OS	*	*	*	*	*	*
15N	MS vs OS	–	–	*	*	*	*
	CS vs OS	*	*	*	*	*	*

[1] –, no difference exist; ∗, significant difference is observed;

TABLE III

FORCE TRACKING RESULTS IN THE STATIC PHASE (MEDIAN ± SD_{ERR})

		$\boldsymbol{F_{des}} = 7N$		$\boldsymbol{F_{des}} = 15N$	
		Rigid	Soft	Rigid	Soft
S1	MS	7.13 ± 0.21	7.01 ± 0.15	15.01 ± 0.18	15.10 ± 1.83
	CS	3.41 ± 0.03	3.44 ± 0.01	10.72 ± 0.06	12.25 ± 0.08
	OS	**6.49 ± 0.01**	**6.49 ± 0.02**	**14.38 ± 0.02**	**14.10 ± 0.06**
S2	MS	7.10 ± 0.31	7.30 ± 0.26	14.50 ± 0.55	14.40 ± 0.48
	CS	4.39 ± 0.01	3.91 ± 0.02	13.05 ± 0.01	13.14 ± 0.02
	OS	**6.36 ± 0.02**	**6.57 ± 0.02**	**14.86 ± 0.06**	**14.55 ± 0.01**
S3	MS	7.48 ± 0.47	6.79 ± 0.28	15.78 ± 0.75	14.60 ± 0.25
	CS	4.33 ± 0.03	3.67 ± 0.03	13.40 ± 0.01	14.13 ± 0.03
	OS	**6.36 ± 0.01**	**6.50 ± 0.02**	**14.77 ± 0.01**	**14.35 ± 0.06**
S4	MS	6.89 ± 0.18	5.20 ± 0.98	14.99 ± 0.29	14.69 ± 0.12
	CS	4.17 ± 0.01	3.44 ± 0.03	11.21 ± 0.03	11.17 ± 0.04
	OS	**6.31 ± 0.02**	**6.55 ± 0.01**	**14.24 ± 0.01**	**14.48 ± 0.01**
S5	MS	7.11 ± 0.23	7.18 ± 0.15	15.63 ± 0.66	15.35 ± 0.33
	CS	4.10 ± 0.02	3.61 ± 0.03	10.90 ± 0.03	11.17 ± 0.03
	OS	**6.32 ± 0.01**	**6.41 ± 0.02**	**14.44 ± 0.02**	**14.86 ± 0.10**
S6	MS	7.53 ± 0.67	7.55 ± 0.35	14.89 ± 0.27	15.11 ± 0.41
	CS	3.65 ± 0.02	3.43 ± 0.02	11.25 ± 0.09	13.28 ± 0.01
	OS	**6.46 ± 0.01**	**6.34 ± 0.02**	**14.65 ± 0.04**	**14.39 ± 0.01**

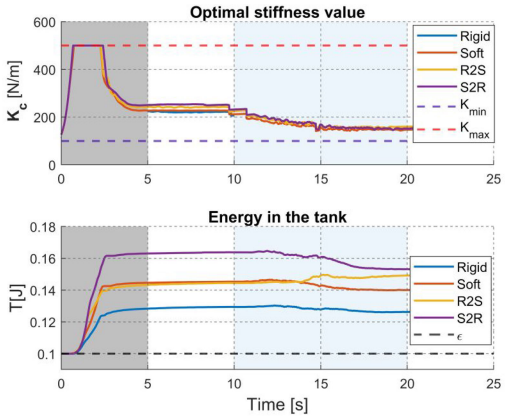

Fig. 7. OS and energy stored in the tank with $\boldsymbol{F}_{\text{des}} = 10$ N.

or estimate, and therefore the CS setup could not track the desired contact force $\boldsymbol{F}_{\text{des}}$; In contrast, OS modality (bottom row in Fig. 6) was capable of tracking the desired force while no significant oscillations occur during the *"holding phase."*

In addition, the RMSE_{err} was calculated for all experimental setups, and the results are shown in Table I. In the *"holding phase"* of the contact task, the MS, CS, and OS modalities gave maximum RMSE_{err} as 0.59, 3.81, and 0.88 N, respectively. Furthermore, the statistical analysis of the difference between the modalities was investigated, as illustrated in Table II. From the Table II, no significant difference existed in MS vs OS, in all three different levels of desired force $\boldsymbol{F}_{\text{des}}$, indicating that the proposed OS strategy was able to achieve comparable performance as MS. This is because the operator adjusts the desired contact force by observing the T/F sensor value within 0–5 s in the *"initialization phase"* and then holding it with small fluctuations. However, significant differences were observed in the comparison setups of CS versus OS, depicting that the Cartesian impedance controller's CS value setup is incapable of tracking $\boldsymbol{F}_{\text{des}}$.

Furthermore, Table III gives the results of Median and SD_{err} in the *"static contact"* tasks with desired contact forces 7 and 15 N. The results are similar to the ones in Tables I and II, and a lower SD_{err} of the tracking error can be observed in CS and OS modalities, which indicates that more standardized results are achieved by leveraging the capability of the robotic system and the proposed OS control strategy.

B. Experiment Results in Scanning Phase of Contact Task

The cyan-blue background in Fig. 6 illustrates the detailed force-tracking curves over the 10 s sampling time (from 10–20 s). Similar to the results during the *"holding phase"* with the gray background, significant variations of the contact

TABLE IV
FORCE TRACKING PERFORMANCE IN MEDICAL CONTACT TASKS ON DIFFERENT MATERIALS (MEDIAN ± SD_{ERR})

Subject	Setups	$F_{des} = 7N$				$F_{des} = 15N$			
		Rigid	Soft	R2S	S2R	Rigid	Soft	R2S	S2R
S1	MS	6.61 ± 0.81	7.93 ± 0.77	7.42 ± 1.87	8.66 ± 1.38	12.07 ± 1.94	13.08 ± 1.98	16.32 ± 1.13	15.10 ± 1.83
	CS	7.52 ± 1.48	7.50 ± 1.24	7.88 ± 1.35	8.13 ± 1.40	17.01 ± 2.31	18.20 ± 1.95	18.02 ± 1.59	17.38 ± 2.21
	OS	**6.86 ± 0.24**	**6.93 ± 0.31**	**7.02 ± 0.34**	**6.74 ± 0.25**	**14.81 ± 0.29**	**14.61 ± 0.35**	**14.76 ± 0.38**	**15.01 ± 0.43**
S2	MS	7.36 ± 1.24	7.84 ± 0.60	5.19 ± 1.33	7.02 ± 0.34	14.56 ± 1.50	16.65 ± 1.06	11.69 ± 1.52	13.60 ± 1.71
	CS	8.41 ± 1.48	8.17 ± 1.59	7.38 ± 1.61	7.31 ± 1.43	16.91 ± 2.19	17.12 ± 2.22	15.85 ± 1.30	16.21 ± 1.17
	OS	**6.89 ± 0.34**	**6.83 ± 0.24**	**6.68 ± 0.17**	**6.97 ± 0.23**	**14.56 ± 0.22**	**14.83 ± 0.42**	**14.51 ± 0.29**	**14.83 ± 0.25**
S3	MS	5.54 ± 1.14	9.66 ± 1.23	7.01 ± 1.01	7.43 ± 0.33	16.02 ± 1.08	15.68 ± 1.65	14.98 ± 2.40	15.14 ± 0.56
	CS	7.62 ± 1.59	7.55 ± 1.61	7.86 ± 1.56	7.75 ± 1.62	16.21 ± 1.17	15.52 ± 1.60	15.69 ± 1.59	16.74 ± 1.35
	OS	**6.57 ± 0.21**	**7.17 ± 0.29**	**6.65 ± 0.18**	**6.61 ± 0.21**	**14.64 ± 0.26**	**14.75 ± 0.27**	**14.33 ± 0.25**	**14.61 ± 0.23**
S4	MS	6.46 ± 0.72	6.81 ± 0.78	7.86 ± 1.72	7.23 ± 1.81	12.94 ± 1.63	13.69 ± 2.49	14.51 ± 1.84	14.28 ± 2.31
	CS	7.88 ± 1.39	8.15 ± 1.31	8.12 ± 1.61	7.86 ± 1.43	15.88 ± 1.52	15.57 ± 1.52	15.71 ± 0.59	15.69 ± 1.02
	OS	**7.27 ± 0.42**	**7.23 ± 0.39**	**7.24 ± 0.44**	**7.16 ± 0.35**	**14.79 ± 0.30**	**14.45 ± 0.38**	**14.72 ± 0.30**	**14.46 ± 0.32**
S5	MS	7.51 ± 0.56	7.96 ± 0.97	6.65 ± 0.32	7.12 ± 0.32	15.12 ± 0.98	15.18 ± 0.94	12.91 ± 1.53	11.98 ± 1.44
	CS	8.70 ± 1.59	7.98 ± 1.53	7.88 ± 1.72	8.51 ± 1.92	16.68 ± 0.55	16.45 ± 0.70	16.03 ± 1.42	16.27 ± 1.39
	OS	**6.94 ± 0.33**	**7.32 ± 0.39**	**7.04 ± 0.38**	**6.7 ± 0.23**	**14.51 ± 0.33**	**14.53 ± 0.33**	**14.83 ± 0.32**	**14.99 ± 0.29**
S6	MS	6.98 ± 1.31	9.10 ± 1.50	7.07 ± 1.04	7.06 ± 1.05	13.64 ± 2.07	13.69 ± 1.86	15.24 ± 1.67	15.36 ± 1.57
	CS	8.35 ± 2.08	8.34 ± 2.01	8.56 ± 2.04	8.54 ± 1.84	15.94 ± 1.53	16.06 ± 1.38	16.85 ± 1.26	15.70 ± 1.50
	OS	**7.24 ± 0.41**	**6.96 ± 0.31**	**7.22 ± 0.41**	**7.24 ± 0.42**	**15.00 ± 0.31**	**14.78 ± 0.41**	**14.68 ± 0.40**	**14.86 ± 0.32**

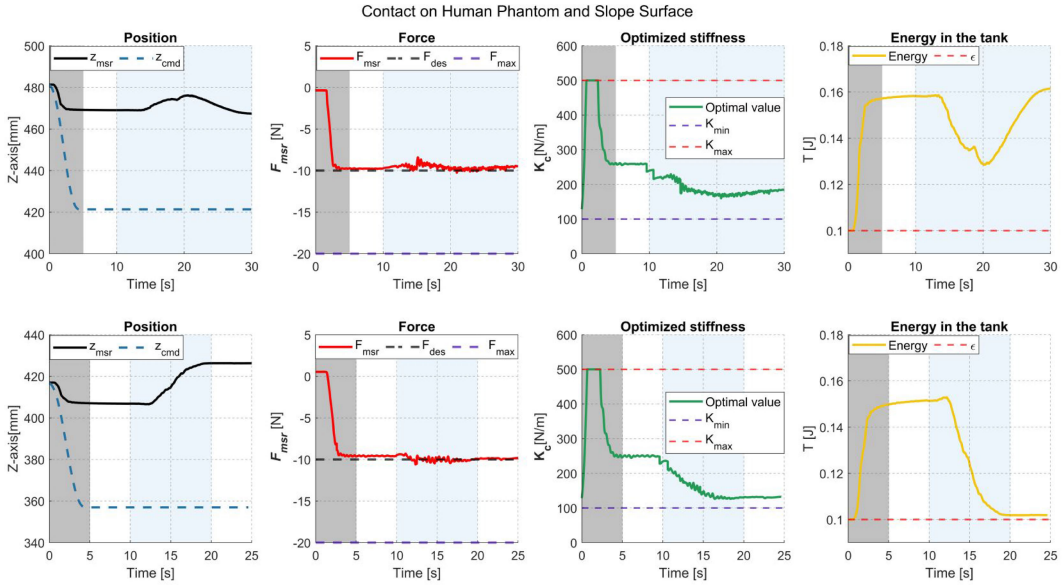

Fig. 8. Experimental results during the contact tasks on the human torso phantom and the slope surface with $F_{des} = 10$ N.

force in the MS modality were shown during the scanning phase of the contact tasks. Conversely, no significant fluctuations were observed in the setups of both CS and OS modalities. However, the CS setup cannot track the desired contact force, as illustrated in Fig. 6, which is because the phantom is not perfectly flat and the deformation issues are caused by material properties.

Also, the $RMSE_{err}$ of the desired force was calculated for the *"scanning phase,"* as depicted in Table I. The maximum $RMSE_{err}$ for the MS, CS, and OS modalities were 2.40, 2.04, and 0.57 N, respectively. Compared with the MS modality in the *"holding phase,"* the $RMSE_{err}$ is higher, indicating that maintaining the force in the dynamic scenario is challenging. On the contrary, the proposed OS strategy exhibits fair performance in the *"scanning phase"* compared to the results in the *"holding phase."* Moreover, as illustrated in Table II, the significant difference was shown in MS versus OS and CS versus OS, indicating that the proposed OS strategy achieved the best performance in all three modalities.

In Fig. 7, the time-varying OS value $\boldsymbol{K_c}(t)$ and the energy $T(x_t)$ in the tank during the contact tasks with OS modality were illustrated. From the subfigure of stiffness value, the robot moved along the z-axis in the *"initialization phase"* to track the desired contact force during 0–5 s, and the stiffness was updated simultaneously. Then, the robot stiffness stayed almost unchanged during the *"holding phase"* at approximately 250 N/m. As shown in Fig. 7, the tests were implemented on four setups (Soft, Rigid, R2S, and S2R), and the stiffness was regulated in the range of [100, 500] N/m. Moreover, from the subfigure of the energy in the tank, the energy stored in the tank was always higher than the threshold value of $\epsilon = 0.1$ J, which indicated that no singularities occurred during the medical contact task execution phase.

In addition, the Median and SD_{err} results during the *"scanning phase"* with 7 and 15 N desired contact force were shown in Table IV. The same as in Table III, including rigid, soft, R2S, and S2R setups. The experimental results showed that

OS modality achieved the best force tracking and stability performance across all the experimental setups.

C. Experiment Results With Uneven Conditions

This section gives the experiment results of contacting with the two uneven conditions, as shown in Fig. 8. The robot stiffness value is still set in the range of [100, 500] N/m. During the period of 0–5 s (gray background), the robot was controlled to move along the Z-axis, and the black curve illustrated the measured Z-axis position. The force curve showed how the contact force changed during the *"initialization phase"*; The stiffness value started from 100 N/m and went to 500 N/m drastically, and decreased afterward when the displacement along Z-axis became higher. During the period of 5–10 s, the robot stayed in the *"holding phase"* to verify the force tracking capability in static contact tasks (e.g., palpation scenario). After that, during the period of 10–30 s (cyan-blue background, *"scanning phase"*), the probe slides on the surface of the torso phantom and tracks the desired force simultaneously. The robot could track the desired contact force by changing the robot stiffness while keeping system passivity, as illustrated by the curve of the energy stored in the tank in Fig. 8.

In the bottom row of Fig. 8, the results of the probe contact with the slope surface were given. The *"initialization phase"* and the *"holding phase"* were similar to the one in the human torso experiment. During the *"scanning phase"* with the period of 10–20 s (cyan-blue background), the measured Z-axis position z_{msr} increased since the probe was scanning on the surface. As illustrated in the stiffness value curve, the robot stiffness value decreased from approximately 250–130 N/m when the displacement between z_{cmd} and z_{msr} increased to track the desired contact force. This indicated that the proposed OS strategy could handle these uneven conditions, simultaneously considering the desired force regulation, complaint behavior, and system stability.

VI. Conclusion

In this study, a novel optimization-based variable impedance control strategy is implemented on a robotic manipulator for medical contact tasks. Experiments are designed to evaluate its performance of force tracking and stability in static contact and scanning tasks on different materials, such as rigid, soft, rigid to soft, and from soft to rigid. The experimental results demonstrate that the proposed control strategy successfully integrates the robotic manipulator and exhibits significant potential in reducing the workload of human medical staff during contact tasks such as US scanning and palpation. Future work will implement adaptive strategies to tune the impedance controller parameters in complex and challenging medical tasks, such as puncture and cutting tasks.

References

[1] Y. Yan and J. Pan, "Fast localization and segmentation of tissue abnormalities by autonomous robotic palpation," *IEEE Robot. Autom. Lett.*, vol. 6, no. 2, pp. 1707–1714, Apr. 2021.

[2] Z. Jiang et al., "Precise repositioning of robotic ultrasound: Improving registration-based motion compensation using ultrasound confidence optimization," *IEEE Trans. Instrum. Meas.*, vol. 71, pp. 1–11, 2022.

[3] G. Faoro, S. Maglio, S. Pane, V. Iacovacci, and A. Menciassi, "An artificial intelligence-aided robotic platform for ultrasound-guided transcarotid revascularization," *IEEE Robot. Autom. Lett.*, vol. 8, no. 4, pp. 2349–2356, Apr. 2023.

[4] D. Huang, C. Yang, M. Zhou, A. Karlas, N. Navab, and Z. Jiang, "Robot-assisted deep venous thrombosis ultrasound examination using virtual fixture," *IEEE Trans. Autom. Sci. Eng.*, early access, doi: 10.1109/TASE.2024.3351076.

[5] J. Fu et al., "Augmented reality-assisted robot learning framework for minimally invasive surgery task," in *Proc. IEEE Int. Conf. Robot. Autom. (ICRA)*, May 2023, pp. 11647–11653.

[6] E. Iovene et al., "Towards exoscope automation in neurosurgery: A markerless visual-servoing approach," *IEEE Trans. Med. Robot. Bionics*, vol. 5, no. 2, pp. 411–420, May 2023, doi: 10.1109/TMRB.2023.3258524.

[7] Y. Huang, W. Xiao, C. Wang, H. Liu, R. Huang, and Z. Sun, "Towards fully autonomous ultrasound scanning robot with imitation learning based on clinical protocols," *IEEE Robot. Autom. Lett.*, vol. 6, no. 2, pp. 3671–3678, Apr. 2021.

[8] J. Zhu et al., "Challenges and outlook in robotic manipulation of deformable objects," *IEEE Robot. Autom. Mag.*, vol. 29, no. 3, pp. 67–77, Sep. 2022.

[9] X. Bao, S. Wang, L. Zheng, R. J. Housden, J. V. Hajnal, and K. Rhode, "A novel ultrasound robot with force/torque measurement and control for safe and efficient scanning," *IEEE Trans. Instrum. Meas.*, vol. 72, pp. 1–12, 2023.

[10] J. Tan et al., "A flexible and fully autonomous breast ultrasound scanning system," *IEEE Trans. Autom. Sci. Eng.*, vol. 20, no. 3, pp. 1920–1933, Jul. 2023, doi: 10.1109/TASE.2022.3189339.

[11] J. Zhang, Y. Wang, T. Liu, K. Yang, and H. Jin, "A flexible ultrasound scanning system for minimally invasive spinal surgery navigation," *IEEE Trans. Med. Robot. Bionics*, vol. 3, no. 2, pp. 426–435, May 2021.

[12] N. Hogan, "Impedance control: An approach to manipulation," in *Proc. Amer. Control Conf.*, 1984, pp. 304–313.

[13] J. Fu et al., "Augmented reality and human–robot collaboration framework for percutaneous nephrolithotomy: System design, implementation, and performance metrics," *IEEE Robot. Autom. Mag.*, doi: 10.1109/MRA.2024.3358721.

[14] Z. Jiang, Y. Zhou, Y. Bi, M. Zhou, T. Wendler, and N. Navab, "Deformation-aware robotic 3D ultrasound," *IEEE Robot. Autom. Lett.*, vol. 6, no. 4, pp. 7675–7682, Oct. 2021.

[15] J. Tan et al., "Automatic generation of autonomous ultrasound scanning trajectory based on 3-D point cloud," *IEEE Trans. Med. Robot. Bionics*, vol. 4, no. 4, pp. 976–990, Nov. 2022.

[16] L. Biagiotti, R. Meattini, D. Chiaravalli, G. Palli, and C. Melchiorri, "Robot programming by demonstration: Trajectory learning enhanced by sEMG-based user hand stiffness estimation," *IEEE Trans. Robot.*, vol. 39, no. 4, pp. 3259–3278, Aug. 2023, doi: 10.1109/TRO.2023.3258669.

[17] R. Martín-Martín, M. A. Lee, R. Gardner, S. Savarese, J. Bohg, and A. Garg, "Variable impedance control in end-effector space: An action space for reinforcement learning in contact-rich tasks," in *Proc. IEEE/RSJ Int. Conf. Intell. Robots Syst. (IROS)*, Nov. 2019, pp. 1010–1017.

[18] L. Roveda, N. Iannacci, F. Vicentini, N. Pedrocchi, F. Braghin, and L. M. Tosatti, "Optimal impedance force-tracking control design with impact formulation for interaction tasks," *IEEE Robot. Autom. Lett.*, vol. 1, no. 1, pp. 130–136, Jan. 2016.

[19] J. Zhao, A. Giammarino, E. Lamon, J. M. Gandarias, E. D. Momi, and A. Ajoudani, "A hybrid learning and optimization framework to achieve physically interactive tasks with mobile manipulators," *IEEE Robot. Autom. Lett.*, vol. 7, no. 3, pp. 8036–8043, Jul. 2022.

[20] C. Secchi, S. Stramigioli, and C. Fantuzzi, *Control of Interactive Robotic Interfaces: A Port-Hamiltonian Approach*, vol. 29. Cham, Switzerland: Springer, 2007.

[21] F. Ferraguti et al., "An energy tank-based interactive control architecture for autonomous and teleoperated robotic surgery," *IEEE Trans. Robot.*, vol. 31, no. 5, pp. 1073–1088, Oct. 2015.

[22] D. Lee and K. Huang, "Passive-set-position-modulation framework for interactive robotic systems," *IEEE Trans. Robot.*, vol. 26, no. 2, pp. 354–369, Apr. 2010.

[23] C. Hennersperger et al., "Towards MRI-based autonomous robotic US acquisitions: A first feasibility study," *IEEE Trans. Med. Imag.*, vol. 36, no. 2, pp. 538–548, Feb. 2017.

Open Access funding provided by 'Politecnico di Milano' within the CRUI CARE Agreement